

Crystal Structure Prediction and Phase Stability in Highly Anharmonic Silver-Based Chalcohalide Antiperovskites

Pol Benítez^{1,2}, Cibrán López,^{1,2} Cong Liu,³ Ivan Caño,^{2,4} Josep-Lluís Tamarit^{1,2},
Edgardo Saucedo,^{2,4} and Claudio Cazorla^{1,2,*}

¹Group of Characterization of Materials, Departament de Física, Universitat Politècnica de Catalunya,
Campus Diagonal-Besòs, Av. Eduard Maristany 10–14, Barcelona 08019, Spain

²Research Center in Multiscale Science and Engineering, Universitat Politècnica de Catalunya,
Campus Diagonal-Besòs, Av. Eduard Maristany 10–14, Barcelona 08019, Spain

³Departament de Física, Universitat Politècnica de Catalunya, Campus Nord, Jordi Girona 1–3,
Barcelona 08005, Spain

⁴Department of Electronic Engineering, Universitat Politècnica de Catalunya, Barcelona 08034, Spain

(Received 28 October 2024; revised 31 January 2025; accepted 6 March 2025; published 3 April 2025)

Silver-based chalcohalide antiperovskites (CAPs), Ag_3BC ($B = \text{S}, \text{Se}$; $C = \text{Cl}, \text{Br}, \text{I}$), represent an emerging family of energy materials with intriguing optoelectronic, vibrational, and ionic transport properties. However, the structural features and phase stability of CAP remain poorly investigated to date, hindering their fundamental understanding and potential integration into technological applications. Here we employ theoretical first-principles methods based on density-functional theory to fill this knowledge gap. Through crystal-structure prediction techniques, *ab initio* molecular dynamics simulations, and quasiharmonic free-energy calculations, we unveil a series of previously overlooked energetically competitive phases and temperature-induced phase transitions for all CAP. Specifically, we identify a new cubic $P2_13$ structure as the stable phase of all CAP containing S both at zero temperature and $T \neq 0$ K conditions. Consequently, our calculations suggest that the cubic $Pm\bar{3}m$ phase identified in room-temperature x-ray diffraction experiments is possibly metastable. Furthermore, for CAP containing Se, we propose different orthorhombic ($Pca2_1$ and $P2_12_12_1$) and cubic ($I2_13$) structures as the ground-state phases and reveal several phase transformations induced by temperature. This theoretical investigation not only identifies new candidate ground-state phases and solid-solid phase transformations for all CAP but also provides insights into potential stability issues affecting technological applications based on these highly anharmonic materials.

DOI: 10.1103/PRXEnergy.4.023002

I. INTRODUCTION

Silver-based chalcohalide antiperovskites (CAPs) with chemical formula Ag_3BC ($B = \text{S}, \text{Se}$; $C = \text{Cl}, \text{Br}, \text{I}$) are structurally similar to the lead halide perovskites (e.g., CsPbI_3), with the “anti” designation indicating the exchange of anions and cations compared to the typical ionic perovskite arrangement. Analogous to lead halide perovskites, CAPs are highly promising materials for energy and optoelectronic applications, boasting low toxicity due to their lead-free composition [1,2]. The

two most extensively studied CAP compounds, Ag_3SBr and Ag_3SI , possess experimental band gaps of approximately 1.0 eV [3,4], rendering them favorable for photovoltaic applications. These have also been recognized as room-temperature superionic conductors [5,6]. Additionally, CAPs have been investigated as potential thermoelectric materials [7,8] owing to their substantial vibrational anharmonicity and intriguing transport properties [9,10].

The current surge in interest in CAP is evident from the recent publication of several experimental works detailing improved synthesis methods. The pioneering synthesis of the archetypal CAP Ag_3SI and Ag_3SBr dates back to 1960, credited to Reuter and Hardel [11]. However, the majority of early CAP synthesis techniques required vacuum conditions, elevated temperatures (>600 K), and prolonged synthesis durations, often spanning during days or even months. More recently, rapid synthesis routes have emerged, enabling the production of

*Contact author: claudio.cazorla@upc.edu

Published by the American Physical Society under the terms of the [Creative Commons Attribution 4.0 International license](#). Further distribution of this work must maintain attribution to the author(s) and the published article's title, journal citation, and DOI.

high-purity Ag_3SI and Ag_3SBr powders at temperatures below 600 K through mechanochemical methods [3]. Furthermore, advancements have also led to the synthesis of CAP solid solutions at moderate temperatures (<500 K), such as $\text{Ag}_3\text{SBr}_{x}\text{I}_{1-x}$ ($0 \leq x \leq 1$), using a cost-effective solution-processing approach [4].

Despite these recent synthesis advances, the phase stability and structural properties of CAP remain poorly investigated and understood to date. For both Ag_3SBr and Ag_3SI , three different polymorphs have been consistently reported: a low-temperature γ phase (<130–160 K), a room-temperature phase denoted as β with low ionic conductivity, and an α phase at high temperatures (>500 K) exhibiting high ionic Ag^+ conductivity and S^-/I^- or S^-/Br^- chemical disorder [12–14]. Regarding Ag_3SCl and the rest of CAP compounds containing Se, to the best of our knowledge, there is no experimental data on their structural and phase-stability properties.

In the original reports by Hoshino *et al.* [12–14], the low-temperature γ phase was described as trigonal with space group $R\bar{3}$ for Ag_3SI , and orthorhombic with space group $Cmcm$ for Ag_3SBr . The room-temperature β phase for both Ag_3SI and Ag_3SBr was identified as cubic with space group $Pm\bar{3}m$ and the high-temperature disordered α phase as cubic with space group $I\bar{m}3m$ [6,15,16]. In addition, a metastable room-temperature phase exhibiting high ionic conductivity, denoted as α^* and obtained through quenching of the α phase, has been reported for Ag_3SI [6,15]. However, subsequent studies on Ag_3SBr suggested that the crystal symmetry of the low-temperature γ phase could be more precisely described as monoclinic or triclinic, rather than orthorhombic [17]. Furthermore, investigations into several $\text{Ag}_3\text{SBr}_{x}\text{I}_{1-x}$ solid solutions revealed that for a range of mixed compositions the low-temperature γ phase was orthorhombic with space group $Pnm2_1$ or $Pnnm$ [17].

Since all existing CAP synthesis methods involve temperatures well above ambient conditions, temperatures at which Ag_3SI and Ag_3SBr exhibit ionic conductivity, it is possible that upon cooling the samples remain dynamically arrested in metastable states characterized by ionic disorder. This phenomenon is originated by the existence of significant energy barriers that hinder the transition towards energetically more favorable ordered phases. A similar behavior has been recently demonstrated for halide hybrid perovskites like $\text{MAPbI}_{3-x}\text{Br}_x$ ($\text{MA} = \text{CH}_3\text{NH}_3$ and $x = 1$ or 2) [18]. This likely tendency poses a significant challenge in identifying truly stable low-temperature phases in CAP. Systematic studies able to precisely evaluate the relative stability of different CAP polymorphs are therefore urgently needed. These investigations are crucial for improving our fundamental understanding of CAP and to properly assess their potential for possible technological applications.

This study uses first-principles density-functional theory to identify stable phases for all CAP compounds at both zero and finite temperatures. Notably, the predicted lowest-energy CAP phases, systematically identified through crystal-structure prediction, *ab initio* molecular dynamics, and quasiharmonic free-energy techniques, differ from those previously reported in experimental studies. Therefore, besides providing original and valuable data for Ag_3SCl and other CAP compounds containing Se, the present study prompts a reassessment of the phase diagrams for Ag_3SI and Ag_3SBr , urging further experimental investigations into CAP.

II. RESULTS

A. Zero-temperature crystal-structure prediction

We conducted zero-temperature crystal-structure prediction (CSP) calculations [19–22] for the two archetypal CAP compounds, Ag_3SBr and Ag_3SI , using the MAGUS software [23] and considering a maximum of 20 atoms per unit cell (Methods). MAGUS employs an evolutionary algorithm augmented with machine-learning techniques and graph theory. The initial structures proposed by MAGUS were subsequently relaxed using first-principles methods based on density-functional theory (DFT, Methods). Figure 1 illustrates some of the energetically most favorable phases identified in the rankings resulting from our CSP-DFT calculations (additional structural representations can be found in Fig. S1 within the Supplemental Material [24]). Notable among them are two distinct cubic structures with space group $P2_13$, an orthorhombic $P2_12_12_1$ phase, a monoclinic $P2_1$ phase and a trigonal $R\bar{3}$ phase. It is worth noting that these new structures are topologically distinct from the archetypal perovskite structure $Pm\bar{3}m$. The atomic coordinates of all the crystal structures reported in this study can be freely accessed at Ref. [25].

Figure 2 illustrates the energy rankings of polymorphs for Ag_3SBr and Ag_3SI , as determined using various DFT exchange-correlation energy (E_{xc}) functionals. These include the local density approximation (LDA) [26], the generalized gradient approximation functionals PBE [27] and PBEsol [28], and the strongly constrained and appropriately normed functional (SCAN) [29]. This diverse set of E_{xc} functionals, spanning local and semilocal approximations, facilitates the identification of potential limitations in the employed DFT methods [30].

For Ag_3SBr , all the examined DFT functionals consistently identify the cubic $P2_13$ (I) structure as the ground-state phase [Fig. 2(a)]. At $T = 0$ K, the second energetically most favorable structure is an orthorhombic $P2_12_12_1$ phase, followed by a cubic $P2_13$ (II) and a trigonal $R\bar{3}$ phase. Notably, the PBE functional is the sole functional predicting the cubic $P2_13$ (II) phase to be marginally more favorable than the orthorhombic $P2_12_12_1$ phase. Incorporating spin-orbit coupling (SOC) effects in

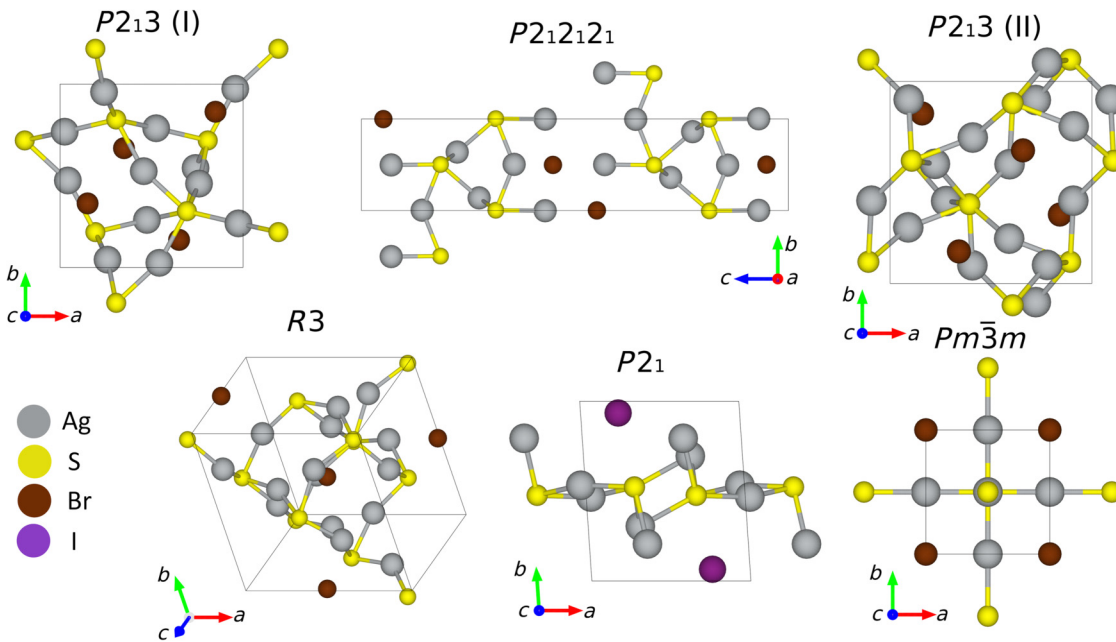


FIG. 1. Sketch of some energetically competitive crystal structures predicted with CSP-DFT methods for the archetypal silver-based chalcohalide antiperovskites Ag_3SBr and Ag_3SI . The cubic $Pm\bar{3}m$ phase that has been experimentally identified as the corresponding room-temperature β phase is shown for comparison. Additional representations of other energetically competitive crystal structures are provided in Fig. S1 within the Supplemental Material [24].

the DFT calculations appears inconsequential, as illustrated by the similarity between the PBEsol and PBEsol + SOC curves. Importantly, our crystal CSP-DFT calculations neither classify the orthorhombic $Cmcm$ nor the cubic $Pm\bar{3}m$ phases as energetically competitive, despite their proposal as the γ and β phases of Ag_3SBr based on experiments [12–14]. Consistently, across all the examined DFT functionals, the energy of these two phases are several hundreds of meV per formula unit (f.u.) higher than that of the theoretical ground state, the cubic $P2_13$ (I) phase [Fig. 2(a)].

For Ag_3SI , the energy ranking is also dominated by the cubic $P2_13$ (I) phase, closely followed by a monoclinic $P2_1$ phase [Fig. 2(b)]. However, the PBE functional deviates from the other energy functionals, suggesting an orthorhombic $P2_12_12_1$ phase as the ground state. Accounting for SOC effects in the DFT calculations neither poses a significant variation in the energy difference results, as evidenced by the nearly identical curves for PBEsol and PBEsol+SOC. Another cubic $P2_13$ (II) phase emerges as energetically competitive across all surveyed DFT functionals. Likewise to Ag_3SBr , the energy of the experimentally observed low-temperature trigonal $R3$ and room-temperature cubic $Pm\bar{3}m$ phases of Ag_3SI are estimated to be substantially higher than that of the corresponding ground-state phase (>0.1 eV/f.u.) by all the examined functionals. It is worth noting the similarity in energy among the trigonal $P3_2$ and $P3_1$ phases identified in our CSP-DFT calculations and the experimentally identified

trigonal $R3$ phase, which stems from their structural resemblance.

Figures 3 and 4 show the vibrational phonon spectra calculated for the four most energetically favorable structures determined for Ag_3SBr and Ag_3SI at zero temperature, respectively, along with those of the cubic $Pm\bar{3}m$ phase and another cubic $I2_13$ phase introduced in the next section. Across the four predicted stable polymorphs, we observe no imaginary phonon frequencies along their high-symmetry reciprocal space paths, indicating their vibrational stability. Interestingly, all these phases exhibit a wide frequency band gap spanning approximately from 5.0 to 7.5 THz, with the exception of the orthorhombic $P2_12_12_1$ phase that displays slightly lower frequencies in the high-frequency regime. Analysis of the phonon spectrum of Ag_3SBr in the cubic $P2_13$ (I) phase shows that modes with energies above the phonon band gap mainly are associated with S vibrations while phonons with energies below the band gap are dominated by Ag and Br atoms (Fig. S2 within the Supplemental Material [24]).

Conversely, the cubic $Pm\bar{3}m$ phase, proposed as the room-temperature β phase of both Ag_3SBr and Ag_3SI [13,14], exhibits numerous imaginary phonon frequencies along all high-symmetry reciprocal space paths, indicating its vibrational instability at $T = 0$ K. A possible T -induced stabilization of this cubic $Pm\bar{3}m$ phase will be discussed further in Sec. III. Additionally, the orthorhombic $Cmcm$ phase (Fig. S3 within the Supplemental Material [24]), suggested as the low-temperature γ phase of Ag_3SBr

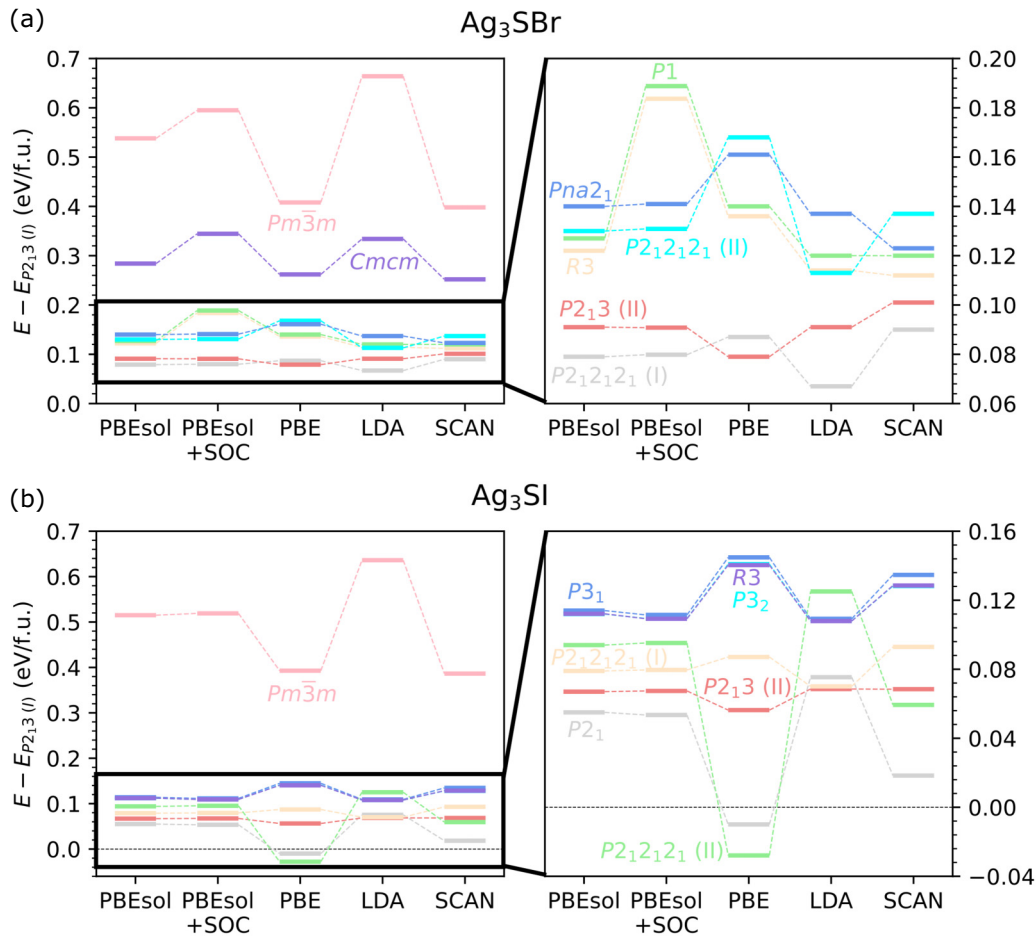


FIG. 2. Energy of competitive crystal structures calculated for archetypal CAP using different DFT exchange-correlation functionals. (a) Ag_3SBr and (b) Ag_3SI . The energy of the cubic $Pm\bar{3}m$ phase that is experimentally resolved at room temperature is shown for comparison. The most relevant energy difference regions are enlarged.

[13,14], exhibits also abundant imaginary phonon frequencies (Fig. S4 within the Supplemental Material [24]). Consequently, this phase is vibrationally unstable at low temperatures and, even ignoring its highly unfavorable energy, cannot be regarded as the ground-state phase. In contrast, the trigonal $R3$ phase, proposed as the low-temperature γ phase of Ag_3SI [13,14], appears to be vibrationally stable at $T = 0$ K conditions (Fig. S4 within the Supplemental Material [24]); however, in view of its high energy [approximately 0.1 eV/f.u., Fig. 2(b)], this phase should be regarded as metastable in the low-temperature regime.

For completeness, we calculated the electronic band-structure properties of Ag_3SBr and Ag_3SI in the predicted ground state ($P2_13$) and experimentally observed room-temperature phase ($Pm\bar{3}m$), as shown in Fig. S5 within the Supplemental Material [24]. These electronic band-structure calculations were performed using the hybrid HSE06 functional [31], including spin-orbit coupling effects (HSE06+SOC), and based on the equilibrium

structures obtained at the PBEsol level [28]. In all cases, the estimated band gaps were identified as indirect, with values ranging from 1.4 to 1.9 eV (Fig. S5 within the Supplemental Material [24]). Ag_3SBr in the $Pm\bar{3}m$ phase exhibited the largest band gap, while Ag_3SI in the $P2_13$ phase presented the smallest.

As demonstrated in this section, our CSP-DFT calculations yield a significantly different set of candidate ground-state phases compared to those experimentally proposed for Ag_3SBr and Ag_3SI . In our calculations, a cubic $P2_13$ phase emerges as the most energetically favorable phase at low temperatures, followed by either an orthorhombic $P2_12_12_1$ or a monoclinic $P2_1$ phase, depending on the material. Importantly, these new candidate ground-state phases are all shown to be vibrationally stable, contrasting with, for example, the orthorhombic $Cmcm$ phase proposed as the lowest-energy structure of Ag_3SBr . Consequently, our theoretical findings call for a re-evaluation of previous experimental characterizations of CAP conducted at low temperatures.

B. Finite-temperature crystal-structure prediction

The observed low-temperature vibrational instability of the cubic $Pm\bar{3}m$ phase (Figs. 3–4), proposed as the room-temperature β phase of both Ag_3SBr and Ag_3SI [13,14], prompted us to perform comprehensive *ab initio* molecular dynamics (AIMD) simulations at $T \neq 0$ K conditions (Methods). The primary objective of these dynamical simulations was to assess the vibrational stability of this phase at finite temperatures as well as to evaluate its ionic transport properties. All the results presented in what follows, if not stated otherwise, were obtained with the semilocal PBEsol exchange-correlation energy functional [28].

Figure 5 shows the position correlation function, $p(\Delta t)$, and mean square displacement, $\Delta r(\Delta t)$, estimated for Ag_3SBr at $T = 200$ and 600 K. These time-dependent functions are defined as [32,33]

$$p(\Delta t) = \langle [\mathbf{r}_i(\Delta t + t_0) - \mathbf{R}_i^0] \cdot [\mathbf{r}_i(t_0) - \mathbf{R}_i^0] \rangle \quad (1)$$

$$\Delta r^2(\Delta t) = \langle [\mathbf{r}_i(\Delta t + t_0) - \mathbf{r}_i(t_0)]^2 \rangle, \quad (2)$$

where \mathbf{r}_i represents the position vector of atom i , t_0 an arbitrary time origin, \mathbf{R}_i^0 the position vector of the equilibrium lattice site for atom i , and $\langle \dots \rangle$ thermal average performed over particles and time origins.

At $\Delta t = 0$, p is simply the vibrational mean square displacement. The crystal is vibrationally stable if $p(\Delta t \rightarrow \infty) = 0$, because the vibrational displacements at widely

separated times become uncorrelated. Conversely, if the atoms acquire a permanent vibrational displacement, $p(\Delta t \rightarrow \infty)$ becomes nonzero. On the other hand, in the absence of ionic diffusion, Δr^2 converges to a constant equal to twice the vibrational mean square displacement in the limit $\Delta t \rightarrow \infty$. Contrarily, in the presence of ionic diffusion, Δr^2 exhibits a linear dependence on Δt with a positively defined slope at sufficiently long times.

The p and Δr^2 results presented in Fig. 5 indicate that Ag_3SBr in the cubic $Pm\bar{3}m$ phase is vibrationally stable at $T = 200$ K, and exhibits significant Ag ionic diffusion at $T = 600$ K. The slow decay of p and large asymptotic value of Δr^2 estimated for Ag ions at $T = 200$ K indicate high anharmonicity, despite of the low temperature. In contrast, the p and Δr^2 results presented in Fig. 6 indicate a markedly different behavior for Ag_3SI . Specifically, the vibrational centers of Ag ions somewhat change throughout the $T = 200$ K simulation, $\{\mathbf{R}_i^0\} \rightarrow \{\mathbf{R}_i^*\}$, since $p(\Delta t \rightarrow \infty) \neq 0$ for these atoms. Furthermore at high temperatures, the Ag ionic diffusion is appreciably higher in Ag_3SI than in Ag_3SBr .

Figure 7 shows the simulated trajectory of an arbitrary silver ion in Ag_3SBr and Ag_3SI at different temperatures, considering the cubic $Pm\bar{3}m$ phase. At $T = 200$ K, the map of position points is more anisotropic for Ag_3SI than for Ag_3SBr . Specifically, multiple vibrational centers can be identified for Ag_3SI [Fig. 7(b)], whereas they are not observed for Ag_3SBr [Fig. 7(a)]. Notably, the amplitude of

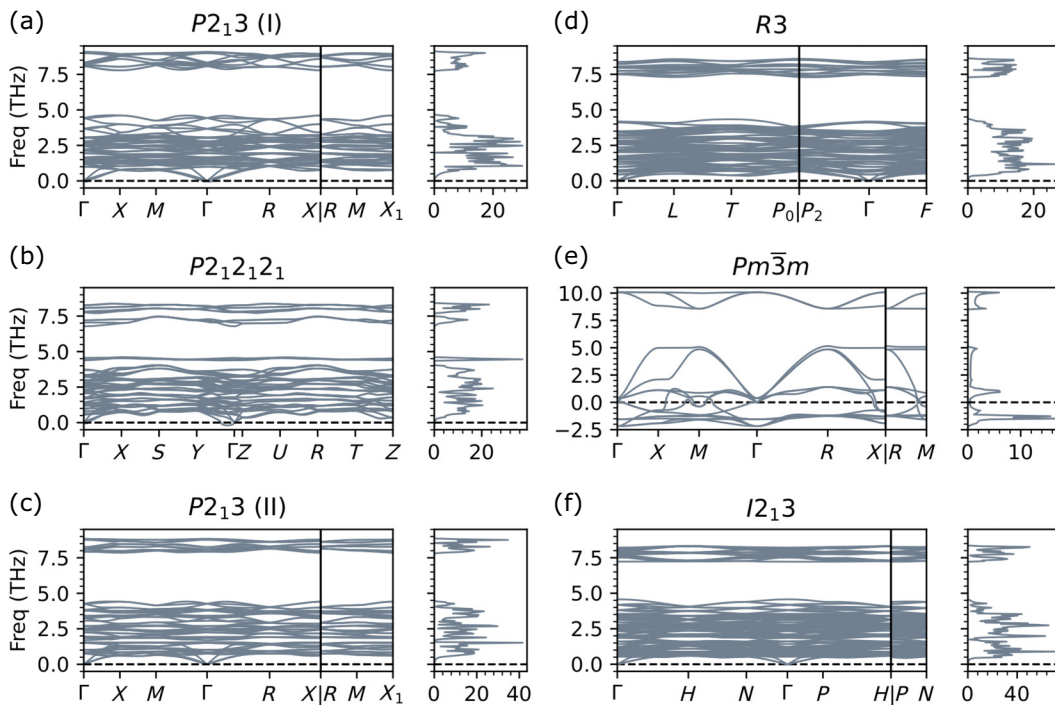


FIG. 3. Vibrational phonon spectrum of Ag_3SBr calculated for different crystal structures. Phonon calculations were performed at zero-temperature conditions. All considered phases are vibrationally except the cubic $Pm\bar{3}m$ phase, which exhibits numerous imaginary phonon branches. Results were obtained with the semilocal functional PBEsol [28].

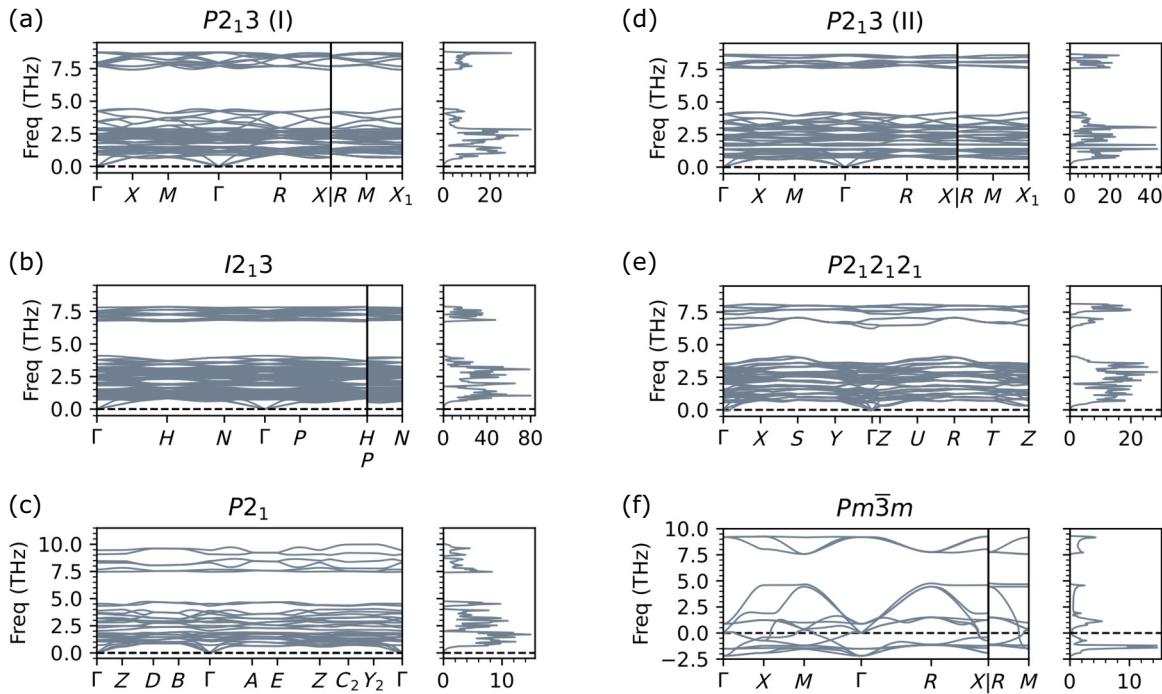


FIG. 4. Vibrational phonon spectrum of Ag_3SI calculated for different crystal structures. Phonon calculations were performed at zero-temperature conditions. All considered phases are vibrationally stable except the cubic $Pm\bar{3}m$ phase, which exhibits numerous imaginary phonon branches. Results were obtained with the semilocal functional PBEsol [28].

the ionic vibrations in Ag_3SBr is very wide, thus denoting high anharmonicity. These observations are consistent with the p results presented in Figs. 5 and 6 for Ag ions.

At $T = 600$ K, on the other hand, silver ionic hoppings are clearly observed in both compounds, illustrating their superionic character at high temperatures.

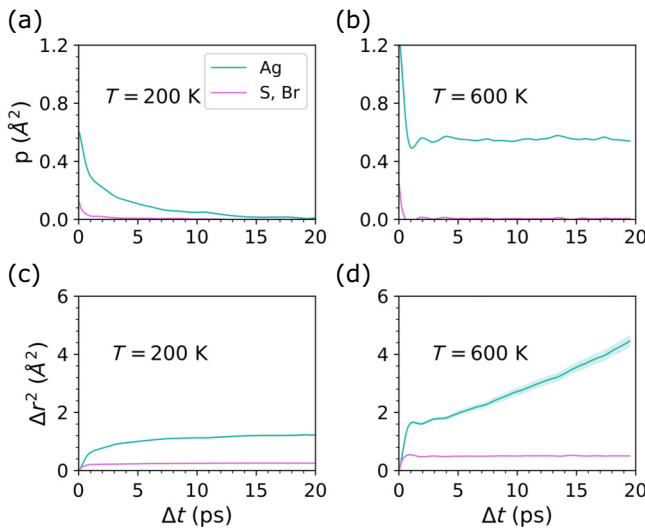


FIG. 5. Analysis of the vibrational stability and ionic diffusion of Ag_3SBr in the cubic $Pm\bar{3}m$ phase at $T \neq 0$ conditions. (a),(b) Position correlation function [32,33], $p(\Delta t)$, estimated at $T = 200$ and 600 K. (c),(d) Mean square displacement, $\Delta r^2(\Delta t)$, estimated at $T = 200$ and 600 K. Results were obtained from *ab initio* molecular dynamics simulations (Methods) performed with the semilocal functional PBEsol [28].

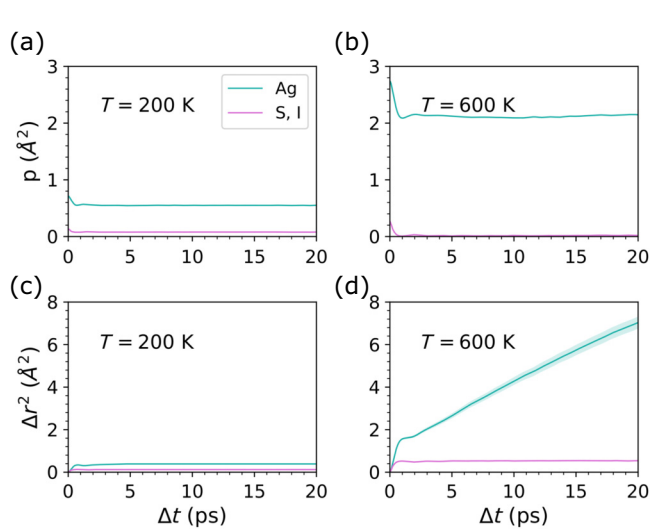


FIG. 6. Analysis of the vibrational stability and ionic diffusion of Ag_3SI in the cubic $Pm\bar{3}m$ phase at $T \neq 0$ conditions. (a),(b) Position correlation function [32,33], $p(\Delta t)$, estimated at $T = 200$ and 600 K. (c),(d) Mean square displacement, $\Delta r^2(\Delta t)$, estimated at $T = 200$ and 600 K. Results were obtained from *ab initio* molecular dynamics simulations (Methods) performed with the semilocal functional PBEsol [28].

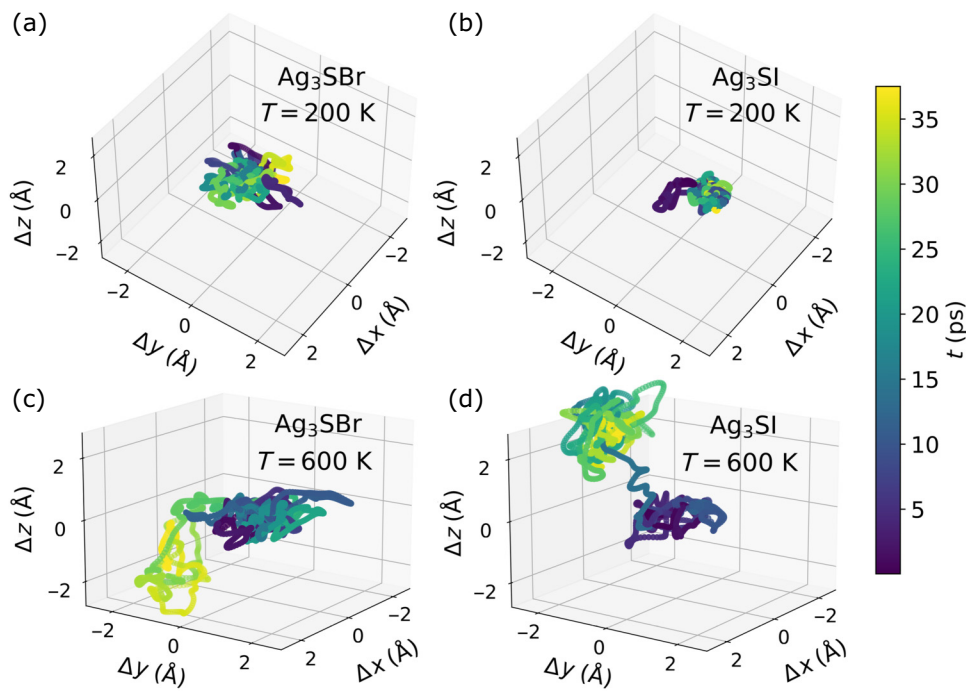


FIG. 7. Analysis of Ag ion trajectories obtained from *ab initio* molecular dynamics simulations. Ag_3SBr in the cubic $Pm\bar{3}m$ phase at (a) $T = 200$ K and (c) $T = 600$ K. Ag_3SI in the cubic $Pm\bar{3}m$ phase at (b) $T = 200$ K and (d) $T = 600$ K. Results were obtained with the semilocal functional PBEsol [28].

The AIMD trajectories of mobile Ag ions were analyzed using the `IonDiff` software [34,35] to elucidate the dominant ionic diffusion mechanisms in CAP (Fig. S6 within the Supplemental Material [24]). Consistent with previous simulation studies on superionic Li-based antiperovskites (e.g., Li_3OCl and Li_3OBr) [36], the identified hopping mechanisms primarily involved the formation of Ag interstitial dumbbells, which are highly concerted [37]. On average, the mobile Ag ions were found to occupy the interstitial positions for approximately 6.9 ps. This analysis highlights the dynamic and coordinated nature of ionic diffusion in CAP.

In an attempt to identify the crystal structure towards which Ag_3SI appears to transform from the cubic $Pm\bar{3}m$ phase, we performed zero-temperature geometry relaxations of a series of supercell configurations extracted from the AIMD runs (Fig. 8). Figure 8(b) shows the lowest-energy configuration obtained through this process, which contains a total of 320 atoms. Using the `FINDSYM` software [38], this supercell was efficiently reduced to a cubic 40-atom primitive cell with space group $I2_13$ [Fig. 8(c)]. Interestingly, this new cubic $I2_13$ phase was found to be vibrationally stable at low temperatures for both Ag_3SBr and Ag_3SI (Figs. 3 and 4). As discussed in the next section, this new cubic $I2_13$ phase was also found to be energetically competitive with respect to the ground-state phases determined for most silver chalcocarbonate antiperovskite.

C. Zero-temperature phase competition

After the detailed study of the structural and vibrational properties of Ag_3SBr and Ag_3SI , we extended our investigation to other materials in the CAP family, namely, Ag_3SCl , Ag_3SeCl , Ag_3SeBr , and Ag_3SeI . It is worth noting that, to the best of our knowledge, there are no experimental reports on these compounds in the literature. For each new CAP, we began by relaxing the 60 lowest-energy phases identified for the archetypal compounds Ag_3SBr and Ag_3SI , using the semilocal PBEsol exchange-correlation energy functional [28]. The cubic $I2_13$ phase discovered from the AIMD simulations performed for Ag_3SI and the experimental room-temperature cubic $Pm\bar{3}m$ phase, were additionally considered in our pool of candidate ground-state phases.

Figure 9 and Table I summarize our zero-temperature DFT structure energy rankings obtained for the CAP family. For Ag_3SBr and Ag_3SI , the primary difference compared to the results in Fig. 2 is the inclusion of the new cubic $I2_13$ phase. This phase has an energy only 45 meV/f.u. higher than the cubic $P2_13$ (I) ground-state phase in Ag_3SI , and approximately 100 meV/f.u. higher than the same ground-state phase in Ag_3SBr . For the analogous Se-based CAP, the cubic $I2_13$ phase is even more relevant; it has the lowest energy for Ag_3SeI , and for Ag_3SeBr its energy is only about 35 meV/f.u. higher than that of the orthorhombic $P2_12_12_1$ ground-state phase (Fig. 9).

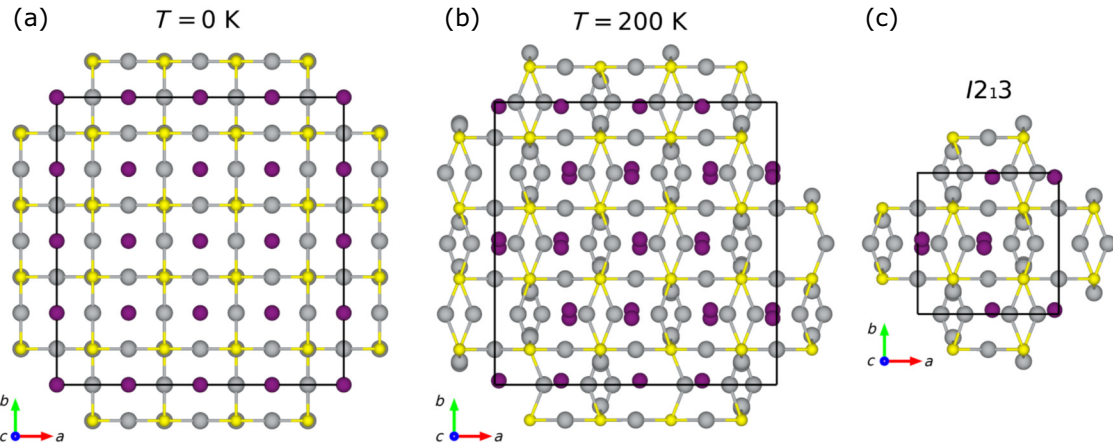


FIG. 8. Ag_3SI supercell representations obtained from *ab initio* molecular dynamics simulations. (a) The starting cubic $Pm\bar{3}m$ phase at zero temperature. (b) The distorted cubic $Pm\bar{3}m$ phase found at $T = 200$ K. (c) The new cubic $I2_13$ phase determined from the distorted cubic $Pm\bar{3}m$ phase. Ag, S, and I ions are represented with gray, yellow, and purple spheres, respectively. Results were obtained with the semilocal functional PBEsol [28].

The ground-state phase of all analyzed S-based CAP corresponds to the cubic $P2_13$ (I) phase, which in the Ag_3Cl system is closely followed by two orthorhombic phases with crystal symmetries $P2_12_12_1$ and $Pca2_1$. Regarding the Se-based CAP, in Ag_3SeCl and Ag_3SeBr , the lowest-energy phases are dominated by orthorhombic phases (e.g., $P2_12_12_1$ and $Pca2_1$), the cubic $I2_13$ phase

being the most significant energy competitor presenting a different crystal symmetry. In the specific case of Ag_3SeI , a trigonal $P3_1$ and a monoclinic $P2_1$ phase were also ranked among the lowest-energy structures.

We computed the lattice phonon spectrum of the experimental room-temperature cubic $Pm\bar{3}m$ phase and the five energetically most favorable structures found for Ag_3Cl ,

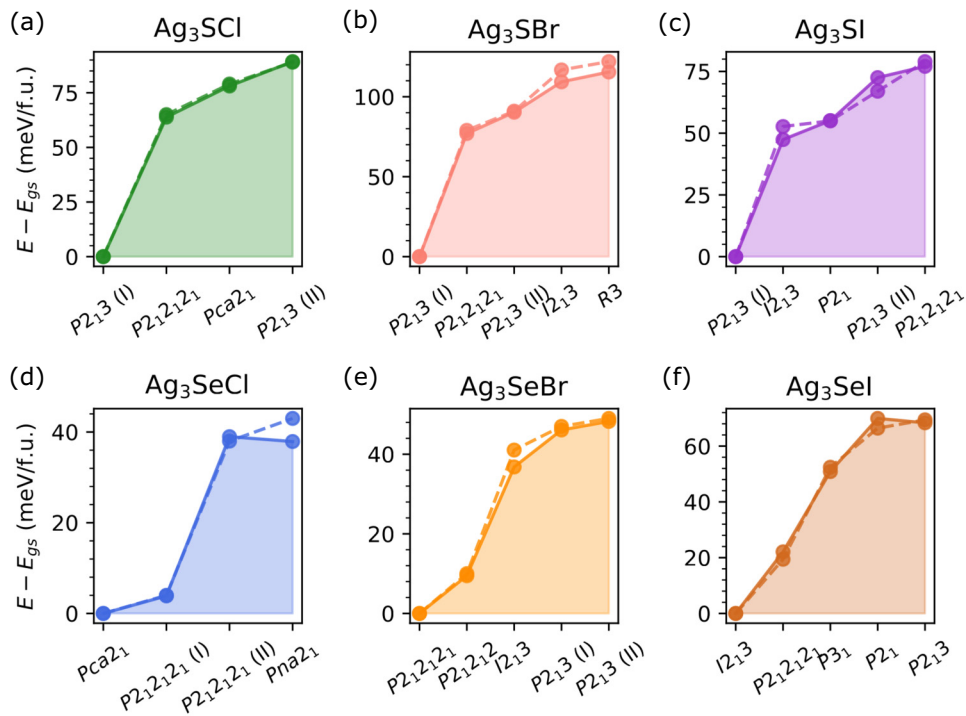


FIG. 9. CAP phase competition determined at zero-temperature conditions. Energy differences neglecting (including) ZPE corrections (Methods) are represented with solid (dashed) lines. Results were obtained with the semilocal functional PBEsol [28]. Energy differences (neglecting ZPE corrections) with respect to the ground state are emphasized with colored areas.

TABLE I. Structural and energy properties of CAP considering several energetically competitive phases. Energy differences, ΔE , are referred to the ground-state phase and expressed in units of meV per formula unit (f.u.). Energy differences including zero-point energy (ZPE) corrections (Methods) are also reported, ΔE^{ZPE} , except for those phases that were found to exhibit imaginary phonon frequencies (indicated as "..."). Results were obtained with the semilocal functional PBEsol [28].

Compound	Structure	Symmetry	a (Å)	b (Å)	c (Å)	α (°)	β (°)	γ (°)	ΔE (meV/f.u.)	ΔE^{ZPE} (meV/f.u.)
Ag_3ScI	Cubic	$P2_13$ (I)	7.478	7.478	7.478	90.000	90.000	90.000	0	0
	Orthorhombic	$P2_12_12_1$	4.502	4.455	20.715	90.000	90.000	90.000	65	64
	Orthorhombic	$Pca2_1$	5.872	9.757	6.877	90.000	90.000	90.000	79	78
	Cubic	$P2_13$ (II)	7.499	7.499	7.499	90.000	90.000	90.000	89	89
	Cubic	$I2_13$	9.389	9.389	9.389	90.000	90.000	90.000	181	...
	Cubic	$Pm\bar{3}m$	4.750	4.750	4.750	90.000	90.000	90.000	627	...
Ag_3SBr	Cubic	$P2_13$ (I)	7.586	7.586	7.586	90.000	90.000	90.000	0	0
	Orthorhombic	$P2_12_12_1$	4.518	4.531	21.152	90.000	90.000	90.000	79	77
	Cubic	$P2_13$ (II)	7.602	7.602	7.602	90.000	90.000	90.000	91	90
	Cubic	$I2_13$	9.446	9.446	9.446	90.000	90.000	90.000	117	109
	Trigonal	$R3$	8.140	8.140	8.140	109.075	109.075	109.075	121	115
	Cubic	$Pm\bar{3}m$	4.793	4.793	4.793	90.000	90.000	90.000	538	...
Ag_3SI	Cubic	$P2_13$ (I)	7.734	7.734	7.734	90.000	90.000	90.000	0	0
	Cubic	$I2_13$	9.568	9.568	9.568	90.000	90.000	90.000	53	47
	Monoclinic	$P2_1$	6.176	6.984	5.656	90.000	90.000	93.869	55	55
	Cubic	$P2_13$ (II)	7.739	7.739	7.739	90.000	90.000	90.000	67	73
	Orthorhombic	$P2_12_12_1$	4.563	4.612	21.767	90.000	90.000	90.000	79	77
	Cubic	$Pm\bar{3}m$	4.869	4.869	4.869	90.000	90.000	90.000	516	...
Ag_3SeCl	Orthorhombic	$Pca2_1$	5.879	10.014	6.980	90.000	90.000	90.000	0	0
	Orthorhombic	$P2_12_12_1$ (I)	4.688	4.475	21.053	90.000	90.000	90.000	4	4
	Orthorhombic	$P2_12_12_1$ (II)	5.761	5.743	12.651	90.000	90.000	90.000	38	39
	Orthorhombic	$Pna2_1$	6.347	6.450	9.966	90.000	90.000	90.000	43	38
	Cubic	$I2_13$	9.626	9.626	9.626	90.000	90.000	90.000	117	...
	Cubic	$Pm\bar{3}m$	4.930	4.930	4.930	90.000	90.000	90.000	1072	...
Ag_3SeBr	Orthorhombic	$P2_12_12_1$ (I)	4.706	4.562	21.452	90.000	90.000	90.000	0	0
	Orthorhombic	$P2_12_12$ (II)	7.530	14.614	4.365	90.000	90.000	90.000	10	9
	Cubic	$I2_13$	9.678	9.678	9.678	90.000	90.000	90.000	41	37
	Cubic	$P2_13$ (I)	7.739	7.739	7.739	90.000	90.000	90.000	47	46
	Cubic	$P2_13$ (II)	7.737	7.737	7.737	90.000	90.000	90.000	49	48
	Cubic	$Pm\bar{3}m$	4.962	4.962	4.962	90.000	90.000	90.000	916	...
Ag_3SeI	Cubic	$I2_13$	9.782	9.782	9.782	90.000	90.000	90.000	0	0
	Orthorhombic	$P2_12_12_1$	4.761	4.653	21.970	90.000	90.000	90.000	19	22
	Trigonal	$P3_1$	6.949	6.949	8.388	90.000	90.000	120.000	52	51
	Monoclinic	$P2_1$	7.708	7.225	15.533	90.000	90.000	144.418	66	70
	Cubic	$P2_13$ (I)	7.978	7.978	7.978	90.000	90.000	90.000	69	68
	Cubic	$Pm\bar{3}m$	5.022	5.022	5.022	90.000	90.000	90.000	842	...

Ag_3SeCl , Ag_3SeBr , and Ag_3SeI (Figs. S7–S10 within the Supplemental Material [24]). Without any exception, we found that the cubic $Pm\bar{3}m$ phase always exhibits abundant imaginary phonon frequencies. The cubic $I2_13$ phase is also vibrationally unstable for Ag_3ScI and Ag_3SeCl at low temperatures (Figs. S7–S8 within the Supplemental Material [24]). However, the remaining phases are perfectly vibrationally stable for all the targeted CAP (Supplemental Material [24], Figs. S7–S10).

For the structures that exclusively exhibited real and positively defined phonon frequencies, we corrected their

zero-temperature energies to account for likely quantum zero-point effects (ZPEs) [39–41]. It is worth noting that applying quasiharmonic (QH) approaches to materials that exhibit imaginary phonon frequencies is neither physically nor mathematically well justified [39]. Thus, any QH result obtained for phases that exhibit imaginary phonon frequencies (e.g., the cubic $Pm\bar{3}m$ phase for all CAP compounds) cannot be rigorously trusted as quantitatively correct [16]. As shown in Fig. 9 and Table I, accounting for quantum ZPE has a practically negligible effect on the energy rankings obtained using classical mechanics. Only in the

specific cases of Ag_3SeCl and Ag_3SeI , quantum ZPE corrections vary the ordering between the third and fourth and the fourth and fifth most energetically favorable phases, respectively.

D. Finite-temperature phase competition

To predict likely T -induced phase transitions across the CAP family, we applied the QH free-energy formalism [39–41] to all the phases reported in Fig. 9 that were vibrationally stable at low temperatures. It is worth emphasizing that applying QH approaches to phases that exhibit imaginary phonon frequencies is neither physically nor mathematically well justified [39]. Consequently, phases like the cubic $Pm\bar{3}m$ and orthorhombic $Cmcm$ in Ag_3SBr , for example, were excluded from our initial phase competition analysis conducted at $T \neq 0$ K conditions (although the thermodynamic stability of some of these phases were subsequently assessed by considering T -renormalized phonons, see next Sec. III).

Figure 10 shows the QH (Helmholtz) free-energy differences estimated as a function of temperature for the six CAP compounds targeted in this study. At a given temperature, the phase exhibiting the lowest free energy (G) is the equilibrium, or stable, phase. The remaining phases, which are vibrationally stable in principle, are considered

metastable. A T -induced phase transition occurs when the free-energy curve of the equilibrium phase crosses the free-energy curve of a metastable phase. The temperature at which this crossing occurs defines the corresponding phase-transition temperature.

For the S-based CAP, we did not find any T -induced phase transition up to 800 K as evidenced by the lack of G curve crossings involving the cubic $P2_13$ (I) phase. Considering higher temperatures probably is not physically meaningful due to the imminent stabilization of the liquid phase [3,4]. Several G curve crossings involving pairs of metastable phases are observed in Figs. 10(b) and 10(c); however, such metastable phase transitions are not of interest in this study. Consequently, according to our QH free-energy DFT calculations, the cubic $P2_13$ (I) phase is the equilibrium, or stable, phase of Ag_3ScI , Ag_3SBr , and Ag_3SI at room temperature (the same conclusion is obtained when considering T -renormalized phonons for the cubic $Pm\bar{3}m$ phase, see next Sec. III).

For the Se-based CAP, the equilibrium between different phases is appreciably affected by temperature. Specifically, we predict two phase transitions for Ag_3SeCl : the first occurs between the two orthorhombic phases $Pca2_1$ and $P2_12_12_1$ (I) at 150 K, and the second between the two orthorhombic phases $P2_12_12_1$ (I) and $Pna2_1$ at 430 K [Fig.

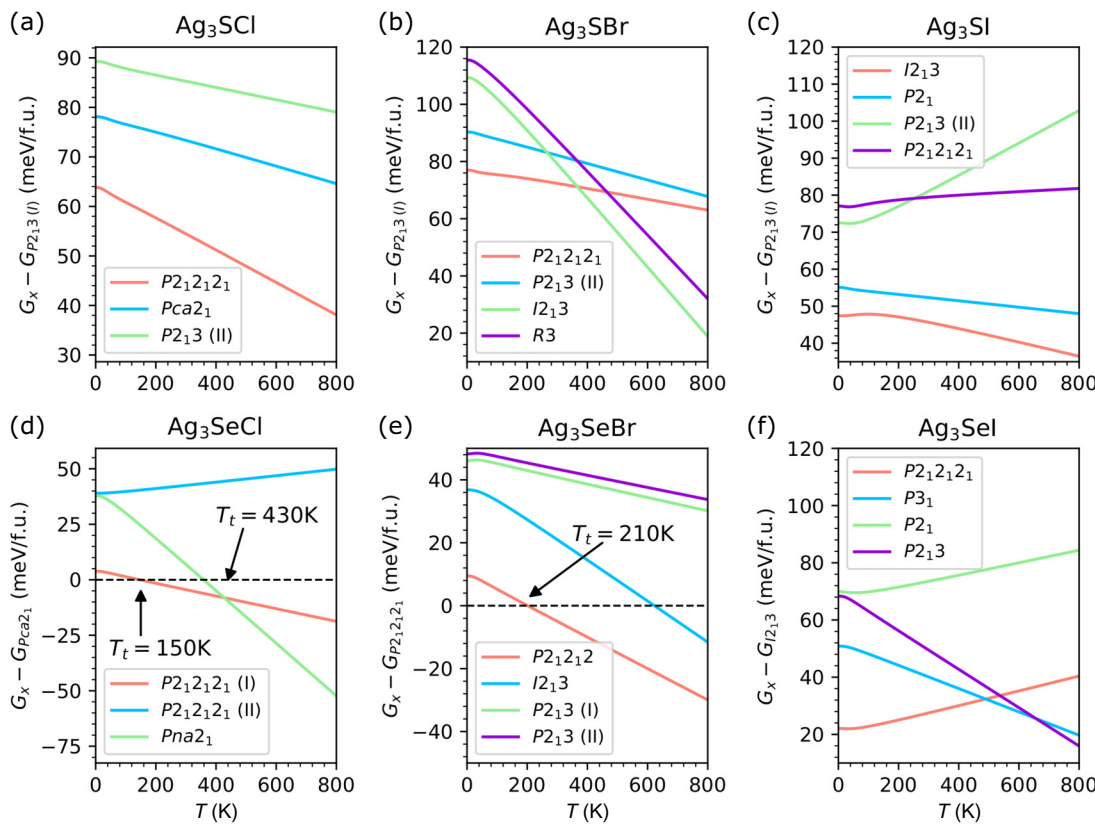


FIG. 10. CAP phase competition determined at $T \neq 0$ conditions. QH Helmholtz free-energy differences, ΔG , were calculated within the quasiharmonic approximation (Methods) [39–41]. Results were obtained with the semilocal functional PBEsol [28].

[10\(d\)](#). For Ag_3SeBr , another phase transition is predicted to occur between the two orthorhombic phases $P2_12_12_1$ (I) and $P2_12_12_1$ (II) at 210 K [Fig. [10\(e\)](#)]. Finally, for Ag_3SeI no T -induced phase transition is observed [Fig. [10\(f\)](#)]. Consequently, according to our QH free-energy DFT calculations, the equilibrium room-temperature phase is orthorhombic $P2_12_12_1$ for Ag_3SeCl and Ag_3SeBr , and cubic $I2_13$ for Ag_3SeI .

III. DISCUSSION

Figure 11 shows the experimental x-ray diffraction patterns obtained for two Ag_3SBr and Ag_3SI polycrystalline samples synthesized through the chemical route detailed in work [\[4\]](#) (Methods). At room temperature, using LeBail phase identification analysis (Methods), the Ag_3SBr film was indexed as cubic $Pm\bar{3}m$ and the Ag_3SI film as cubic $Im\bar{3}m$ (likely due to the presence of ionic disorder). In the same plot, the theoretical x-ray diffraction patterns of several phases obtained from our DFT simulations are included for comparison. The experimental x-ray diffraction pattern of the Ag_3SBr sample perfectly agrees with the theoretical x-ray diffraction pattern of the simulated cubic $Pm\bar{3}m$ phase [Fig. [11\(a\)](#)]. On the other hand, the experimental x-ray diffraction pattern of the Ag_3SI sample cannot be assigned to the theoretical pattern of any single ordered phase [Fig. [11\(b\)](#)].

The experimental x-ray diffraction patterns enclosed in Fig. 11, along with the computational *ab initio* findings presented in the preceding sections, raise the following question: why is the cubic $Pm\bar{3}m$ phase, or the similar one $Im\bar{3}m$, experimentally identified for Ag_3SBr and Ag_3SI at room temperature, instead of the theoretically predicted equilibrium cubic $P2_13$ phase? Although we cannot provide a definitive answer to this question, we can offer some reasonable hypotheses.

First, it is noted that despite the cubic $Pm\bar{3}m$ phase being vibrationally unstable at very low temperatures (Figs. 3 and 4), it could be stabilized under increasing temperature, similar to what is observed in archetypal oxide perovskites [\[42–44\]](#). To evaluate this possibility, we computed the T -renormalized phonon spectrum of this phase for Ag_3SBr and Ag_3SI following a dynamical normal-mode-decomposition technique (Methods) and the Dynaphopy software [\[45\]](#). Using a relatively small $2 \times 2 \times 2$ supercell and a dense \mathbf{k} -point grid for the AIMD simulations ($T = 100$ K) involved in these calculations, to maintain high accuracy and numerical consistency (Supplemental Material [\[24\]](#)), we found that, in fact, the cubic $Pm\bar{3}m$ phase is vibrationally stabilized under increasing temperature (Fig. 12).

Importantly, since no imaginary phonon frequencies appear in the T -renormalized phonon spectra of Ag_3SBr and Ag_3SI (Fig. 12) we can estimate with them the QH free energy of the cubic $Pm\bar{3}m$ phase and compare it with those of other phases. Although not exact, to a first approximation this approach may provide reasonable free-energy results [\[44,46\]](#). Our T -renormalized phonon QH free-energy calculations (Fig. S11 within the Supplemental Material [\[24\]](#)) show that the cubic $Pm\bar{3}m$ phase is not thermodynamically stabilized over the other considered phases at temperatures $T \leq 800$ K since its free energy is never a minimum, in spite of its rapid G decrease observed under increasing temperature. For example, at zero temperature the free-energy difference between the cubic $Pm\bar{3}m$ and ground-state phases approximately amounts to 0.5 eV/f.u. for Ag_3SBr , while at $T = 800$ K this free-energy difference is reduced to 0.1 eV per formula unit.

The substantial free-energy differences between the cubic $Pm\bar{3}m$ structure and the lowest-energy phase (>0.1 eV/f.u.) suggest that our conclusions regarding the thermodynamic metastability of the cubic $Pm\bar{3}m$ phase are unlikely to change, even when employing more advanced

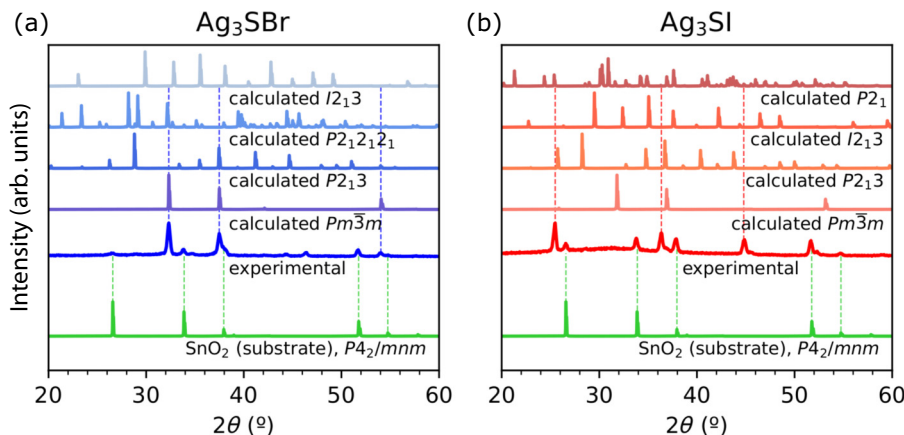


FIG. 11. Experimental x-ray characterization of CAP at room temperature. (a) Ag_3SBr and (b) Ag_3SI . Theoretical DFT results obtained for different energetically competitive phases are shown for comparison.

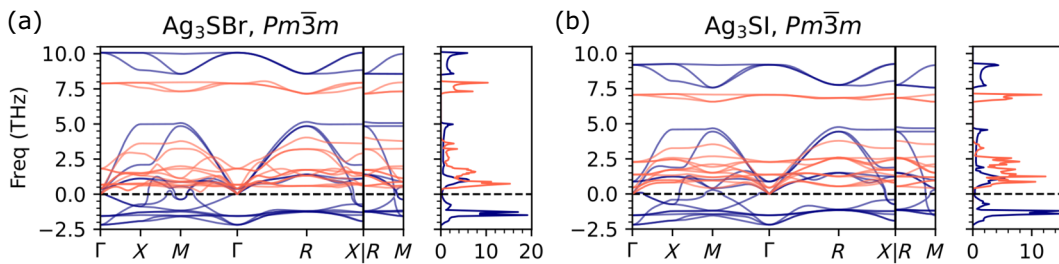


FIG. 12. Temperature-renormalized vibrational phonon spectrum of CAP in the cubic $Pm\bar{3}m$ phase. (a) Ag_3SBr and (b) Ag_3SI . Phonon frequencies obtained at $T = 100$ K (Methods) are represented with orange lines. Zero-temperature phonon frequencies are represented with blue lines. Results were obtained with the semilocal functional PBEsol [28].

and accurate anharmonic free-energy methods [46]. Furthermore, the identification of the cubic $I2_{13}$ phase in our low-temperature AIMD simulations of Ag_3SI , initially in the cubic $Pm\bar{3}m$ phase, further supports this hypothesis.

Based on the presented theoretical findings, our main supposition is that current synthesis methods, all of which involve temperatures significantly higher than 300 K, inevitably trap CAP compounds into metastable states. A key feature, possibly explaining the room-temperature metastability of the synthesized CAP compounds, may be superionicity. According to our AIMD simulations (Figs. S12–S13 within the Supplemental Material [24]), Ag_3SBr in the cubic $Pm\bar{3}m$ phase becomes superionic at $T = 300 \pm 100$ K. On the other hand, the equilibrium cubic $P2_{13}$ phase exhibits negligible ionic diffusivity at room temperature (Fig. S12 within the Supplemental Material [24]). Consequently, it is likely that at temperatures higher than 300 K, such as those involved in CAP synthesis methods, the cubic $Pm\bar{3}m$ phase is further stabilized due to the entropy gain that accompanies ionic diffusion, eventually becoming the equilibrium phase. (Unfortunately, this type of entropy gain resulting from ionic diffusion cannot be reproduced by our QH free-energy DFT calculations.) In that hypothetical case, it seems plausible that upon cooling, the system becomes trapped in the cubic $Pm\bar{3}m$ phase with little possibility to nucleate the equilibrium ordered phase corresponding to ambient temperature.

IV. CONCLUSIONS

For the highly anharmonic and archetypal CAP compounds Ag_3SBr and Ag_3SI , our systematic, comprehensive and technically sound first-principles study suggests a completely different set of stable phases, both at zero temperature and $T \neq 0$ K conditions, compared to what has been proposed from experiments. Specifically, a new cubic $P2_{13}$ phase is found to exhibit the lowest energy at $T = 0$ K and the lowest free energy at finite temperatures, being several hundreds of meV per formula unit lower than the experimentally proposed trigonal $R3$ and orthorhombic $Cmcm$ phases. Additionally, we propose

different ground-state phases and T -induced phase transitions for the less investigated CAP compounds Ag_3SCl , Ag_3SeCl , Ag_3SeBr , and Ag_3SeI .

An intriguing implication of our theoretical findings is that the experimentally observed cubic $Pm\bar{3}m$ phase at room temperature is possibly metastable. Notably, our low-temperature AIMD simulations of Ag_3SI , initially in the cubic $Pm\bar{3}m$ phase, revealed the emergence of a new cubic $I2_{13}$ structure that is both vibrationally stable and energetically competitive with other low-energy polymorphs. The potential metastability of the cubic $Pm\bar{3}m$ phase is likely influenced by the high synthesis temperatures and the onset of superionic behavior above room temperature. It is worth noting that metastable phases have a natural tendency to fluctuate between different energy states, which may pose stability issues for practical technological applications based on CAP. Thus, the present computational study calls for a revision of the prevalent phase diagrams of CAP compounds and motivates new structural characterization experiments conducted under varying temperature conditions, particularly in the low-temperature regime where ionic disorder and metastability can be minimized.

V. METHODS

A. First-principles calculations outline

Ab initio calculations based on DFT [39] were performed to analyze the structural and phase stability properties of CAP. We performed these calculations with the VASP code [47] using different approximations to the exchange-correlation energy, namely, the local and semilocal functionals LDA [26], PBE [27], PBEsol [28], and SCAN [29]. The projector augmented-wave method was used to represent the ionic cores [48] and the following electronic states were considered as valence: Ag 5s 4d, S 3s 3p, Se 4s 4p, Cl 3s 3p, Br 4s 4p, I 5s 5p. Wave functions were represented in a plane-wave basis typically truncated at 650 eV. By using these parameters and dense \mathbf{k} -point grids for reciprocal-space integration (e.g., of $8 \times 8 \times 8$ for the cubic 5-atom $Pm\bar{3}m$ unit cell), the resulting zero-temperature energies were converged to within 1 meV per

formula unit. In the geometry relaxations, a force tolerance of $0.005 \text{ eV } \text{\AA}^{-1}$ was imposed in all the atoms.

B. Harmonic and anharmonic phonon and free-energy calculations

The second-order interatomic force constant of all CAP and resulting harmonic phonon spectrum were calculated with the finite-differences method as is implemented in the Phonopy software [49]. Large supercells (e.g., $4 \times 4 \times 4$ for the cubic $Pm\bar{3}m$ phase containing 320 atoms) and a dense \mathbf{k} -point grid of $3 \times 3 \times 3$ for Brillouin zone (BZ) sampling were employed for the phonon calculations of targeted structures. Several numerical tests were conducted that demonstrated the adequacy of the selected \mathbf{k} -point grid (Fig. S14 within the Supplemental Material [24]). Zero-point energy (ZPE) corrections and finite-temperature Helmholtz free energies (G) were calculated within the quasiharmonic approximation [39–41]. Due to the large number of materials and phases analyzed in this study, thermal expansion effects were disregarded in our ZPE and G calculations.

The DynaPhoPy code [45] was used to calculate the anharmonic lattice dynamics (i.e., T -renormalized phonons) of Ag_3SBr and Ag_3SI in the cubic $Pm\bar{3}m$ phase from *ab initio* molecular dynamics (AIMD) simulations. (For the rest of the phases, which do not exhibit imaginary phonon frequencies, anharmonic lattice dynamics effects were disregarded.) In this case, a reduced $2 \times 2 \times 2$ supercell and $4 \times 4 \times 4$ \mathbf{k} -point grid for BZ sampling were employed in the AIMD simulations to maintain high numerical accuracy (Supplemental Material [24] and Fig. S15).

A normal-mode-decomposition technique was employed in which the atomic velocities $\mathbf{v}_{jl}(t)$ (j and l represent particle and Cartesian direction indexes) generated during fixed-temperature AIMD simulation runs were expressed like

$$\mathbf{v}_{jl}(t) = \frac{1}{\sqrt{Nm_j}} \sum_{\mathbf{q}s} \mathbf{e}_j(\mathbf{q}, s) e^{i\mathbf{q}\mathbf{R}_{jl}^0} v_{\mathbf{q}s}(t), \quad (3)$$

where N is the number of particles, m_j the mass of particle j , $\mathbf{e}_j(\mathbf{q}, s)$ a phonon-mode eigenvector (\mathbf{q} and s stand for the wave vector and phonon branch), \mathbf{R}_{jl}^0 the equilibrium position of particle j , and $v_{\mathbf{q}s}$ the velocity of the corresponding phonon quasiparticle.

The Fourier transform of the autocorrelation function of $v_{\mathbf{q}s}$ then was calculated, yielding the power spectrum:

$$G_{\mathbf{q}s}(\omega) = 2 \int_{-\infty}^{\infty} \langle v_{\mathbf{q}s}^*(0) v_{\mathbf{q}s}(t) \rangle e^{i\omega t} dt. \quad (4)$$

Finally, this power spectrum was approximated by a Lorentzian function of the form:

$$G_{\mathbf{q}s}(\omega) \approx \frac{\langle |v_{\mathbf{q}s}|^2 \rangle}{\frac{1}{2} \gamma_{\mathbf{q}s} \pi \left[1 + \left(\frac{\omega - \omega_{\mathbf{q}s}}{\frac{1}{2} \gamma_{\mathbf{q}s}} \right)^2 \right]}, \quad (5)$$

from which a T -renormalized quasiparticle phonon frequency, $\omega_{\mathbf{q}s}(T)$, was determined as the peak position, and the corresponding phonon linewidth, $\gamma_{\mathbf{q}s}(T)$, as the full width at half maximum.

C. First-principles molecular dynamics simulations

Ab initio molecular dynamics simulations based on DFT were performed in the canonical (N, V, T) ensemble (i.e., constant number of particles, volume, and temperature). The selected volumes were those determined at zero temperature hence thermal-expansion effects were neglected. The temperature in the AIMD simulations was kept fluctuating around a set-point value by using Nose-Hoover thermostats. Large simulation boxes containing $N \sim 200$ –400 atoms were employed (e.g., for the cubic $Pm\bar{3}m$ phase we adopted a $4 \times 4 \times 4$ supercell containing 320 atoms) and periodic boundary conditions were applied along the three supercell lattice vectors. Newton's equations of motion were integrated using the customary Verlet's algorithm with a time step of 1.5×10^{-3} ps. Γ -point sampling for reciprocal-space integration was employed in most of the AIMD simulations, which comprised long simulation times of 80–100 ps.

D. Crystal-structure searches

We used the MAGUS software (Machine learning And Graph theory assisted Universal structure Searcher) [23] to find new candidate stable and metastable phases for the archetypal CAP Ag_3SBr and Ag_3SI . This crystal structure prediction software employs an evolutionary algorithm augmented with machine learning and graph theory to reduce the cost of the geometry optimizations. The crystal phase searches were conducted for structures containing a maximum of 4 formula units (i.e., 20 atoms per unit cell).

E. Experimental procedure

Ag_3SBr and Ag_3SI were synthesized following the chemical route described in work [4]. The samples were characterized by x-ray diffraction using a Bruker D8 advanced diffractometer equipped with a Cu-based tube (40 kV, 40 mA) and a Sol-X detector with discriminator for the K_β line. The measurements were conducted using grazing incidence configuration and the data was analyzed with the LeBail profile fitting method as implemented in the FullProf suite software [50].

ACKNOWLEDGMENTS

C.C. acknowledges support from the Spanish Ministry of Science, Innovation and Universities under the fellowship RYC2018-024947-I and Grant No. PID2023-146623NB-I00. The authors also thankfully acknowledge technical support the computational resources at MareNostrum4 provided by Barcelona Supercomputing Center (FI-2023-1-0002, FI-2023-2-0004, FI-2023-3-0004, and FI-2024-1-0005). P.B. acknowledges support from the Generalitat de Catalunya under a FI Grant. C.L. acknowledges support from the Spanish Ministry of Science, Innovation and Universities under a FPU Grant. This publication and other research outcomes are supported by the predoc-toral program AGAUR-FI ajuts (2024 FI-3 00065) Joan Oró, which is backed by the Secretariat of Universities and Research of the Department of Research and Universities of the Generalitat of Catalonia, as well as the European Social Plus Fund. This work is part of the Maria de Maeztu Units of Excellence Programme CEX2023-001300-M funded by MCIN/AEI (10.13039/501100011033).

DATA AVAILABILITY

The data that support the findings of this study are freely available at the NOMAD data management platform for materials science [51]. These data include the VASP input files of our first-principles DFT calculations as well as some key output files (e.g., relaxed atomic positions of all relevant crystal structures) [25]. The data that support the findings of this article are openly available [25], embargo periods may apply.

- [1] F. Palazon, Metal chalcohalides: Next generation photovoltaic materials? *Sol. RRL* **6**, 2100829 (2022).
- [2] U. V. Ghorpade, M. P. Suryawanshi, M. A. Green, T. Wu, X. Hao, and K. M. Ryan, Emerging chalcohalide materials for energy applications, *Chem. Rev.* **123**, 327 (2023).
- [3] L. Sebastiá-Luna, N. Rodkey, A. S. Mirza, S. Mertens, Melchor Lal, J. Calbo, M. Righetto, M. Sessolo, L. M. Herz, K. Vandewal, E. Ortí, M. Morales-Masis, H. J. Bolink, and F. Palazon, Chalcohalide antiperovskite thin films with visible light absorption and high charge-carrier mobility processed by solvent-free and low-temperature methods, *Chem. Mater.* **35**, 6482 (2023).
- [4] I. Caño, J. W. Turnley, P. Benítez, C. López-Álvarez, J.-M. Asensi, D. Payne, J. Puigdollers, M. Placidi, C. Cazorla, R. Agrawal, and E. Saucedo, Novel synthesis of semiconductor chalcohalide antiperovskites by low-temperature molecular precursor ink deposition methodologies, *J. Mater. Chem. C* **12**, 3154 (2024).
- [5] T. Takahashi and O. Yamamoto, The Ag/Ag₃Si/I₂ solid-electrolyte cell, *Electrochim. Acta* **11**, 779 (1966).
- [6] S. Hull, Superionics: Crystal structures and conduction processes, *Rep. Prog. Phys.* **67**, 1233 (2004).
- [7] J. Kawamura, M. Shimoji, and H. Hoshino, The ionic conductivity and thermoelectric power of the superionic conductor Ag₃SBr, *J. Phys. Soc. Jpn.* **50**, 194 (1981).
- [8] A. Magistris, E. Pezzati, and C. Sinistri, Thermoelectric properties of high-conductivity solid electrolytes, *Z. Naturforsch.* **27a**, 1379 (1972).
- [9] K. Wakamura, F. Miura, A. Kojima, and T. Kanashiro, Observation of anomalously increasing phonon damping constant in the β phase of the fast-ionic conductor Ag₃Si, *Phys. Rev. B* **41**, 2758 (1990).
- [10] T. Sakuma, Treatment of anharmonic thermal vibration by using transformation of scattering vector, *J. Phys. Soc. Jpn.* **54**, 4188 (1985).
- [11] B. Reuter and K. Hardel, Silbersulfidbromid und silbersulfidiodid, *Angew. Chem.* **72**, 138 (1960).
- [12] S. Hoshino, T. Sakuma, and Y. Fujii, The existence of the order phase in superionic conductor Ag₃Si, *J. Phys. Soc. Jpn.* **45**, 705 (1978).
- [13] T. Sakuma and S. Hoshino, The phase transition and the structures of superionic conductor Ag₃SBr, *J. Phys. Soc. Jpn.* **49**, 678 (1980).
- [14] S. Hoshino, H. Fujishita, M. Takashige, and T. Sakuma, Phase transition of Ag₃SX ($X = I, Br$), *Solid State Ionics* **3**, 35 (1981).
- [15] N. Cho, S. Kikkawa, F. Kanamaru, and A. Yoshiasa, Structural refinement of Ag₃Si by single crystal X-ray diffraction method, *Solid State Ionics* **68**, 57 (1994).
- [16] L. Yin, M. Murphy, K. Kim, L. Hu, J. Cabana, D. J. Siegel, and S. H. Lapidus, Synthesis of antiperovskite solid electrolytes: Comparing Li₃Si, Na₃Si and Ag₃Si, *Inorg. Chem.* **59**, 11244 (2020).
- [17] H. Honda, K. Basar, S. Siagian, T. Sakuma, H. Takahashi, H. Kawaji, and T. Atake, Low-temperature phase in superionic conductor Ag₃SBr_xI_{1-x}, *J. Phys. Soc. Jpn.* **76**, 114603 (2007).
- [18] S. Shahrokhi, *et al.*, Anomalous structural evolution and glassy lattice in mixed-halide hybrid perovskites, *Small* **18**, 2200847 (2022).
- [19] R. T. Strong, C. J. Pickard, V. Milman, G. Thimm, and B. Winkler, Systematic prediction of crystal structures: An application to sp 3-hybridized carbon polymorphs, *Phys. Rev. B* **70**, 045101 (2004).
- [20] F. Zahariev, S. V. Dudiy, J. Hooper, F. Zhang, and T. K. Woo, Systematic method to new phases of polymeric nitrogen under high pressure, *Phys. Rev. Lett.* **97**, 155503 (2006).
- [21] X. Shi, C. He, C. J. Pickard, C. Tang, and J. Zhong, Stochastic generation of complex crystal structures combining group and graph theory with application to carbon, *Phys. Rev. B* **97**, 014104 (2018).
- [22] C. He, X. Shi, S. J. Clark, J. Li, C. J. Pickard, T. Ouyang, C. Zhang, C. Tang, and J. Zhong, Complex low energy tetrahedral polymorphs of group IV elements from first principles, *Phys. Rev. Lett.* **121**, 175701 (2018).
- [23] J. Wang, H. Gao, Y. Han, C. Ding, S. Pan, Y. Wang, Q. Jia, H.-T. Wang, D. Xing, and J. Sun, MAGUS: Machine learning and graph theory assisted universal structure searcher, *Nat. Sci. Rev.* **10**, nwad128 (2023).
- [24] See Supplemental Material at <http://link.aps.org/supplemental/10.1103/PRXEnergy.4.023002> for additional information on energetically competitive CAP polymorphs,

- phonon analysis of the cubic $P2_13$ phase, the orthorhombic $Cmcm$ phase, vibrational phonon spectra of Ag_3SBr , electronic band-structure properties of Ag_3SBr and Ag_3SI , ionic diffusivity of Ag_3SBr , vibrational phonon spectra of Ag_3SCl , vibrational phonon spectra of Ag_3SeCl , vibrational phonon spectra of Ag_3SeBr , vibrational phonon spectra of Ag_3SeI , CAP phase competition at $T \neq 0$ K conditions, superionic properties of Ag_3SBr , numerical tests, and a discussion on technical aspects of the AIMD simulations.
- [25] P. Benítez and C. Cazorla, Structural Search Silver Chalcochalide Anti-perovskites, <https://doi.org/10.17172/NOMAD/2024.05.17-2>.
- [26] D. M. Ceperley and B. J. Alder, Ground state of the electron gas by a stochastic method, *Phys. Rev. Lett.* **45**, 566 (1980).
- [27] J. P. Perdew, K. Burke, and M. Ernzerhof, Generalized gradient approximation made simple, *Phys. Rev. Lett.* **77**, 3865 (1996).
- [28] J. P. Perdew, A. Ruzsinszky, G. I. Csonka, O. A. Vydrov, G. E. Scuseria, L. A. Constantin, X. Zhou, and K. Burke, Restoring the density-gradient expansion for exchange in solids and surfaces, *Phys. Rev. Lett.* **100**, 136406 (2008).
- [29] J. Sun, A. Ruzsinszky, and J. P. Perdew, Strongly constrained and appropriately normed semilocal density functional, *Phys. Rev. Lett.* **115**, 036402 (2015).
- [30] D. Meggiolaro and F. De Angelis, First-principles modeling of defects in lead halide perovskites: Best practices and open issues, *ACS Energy Lett.* **3**, 2206 (2018).
- [31] A. V. Krukau, O. A. Vydrov, A. F. Izmaylov, and G. E. Scuseria, Influence of the exchange screening parameter on the performance of screened hybrid functionals, *J. Chem. Phys.* **125**, 224106 (2006).
- [32] C. Cazorla, D. Alfè, and M. J. Gillan, Constraints on the phase diagram of molybdenum from first-principles free-energy calculations, *Phys. Rev. B* **85**, 064113 (2012).
- [33] C. Cazorla and D. Errandonea, Superionicity and polymorphism in calcium fluoride at high pressure, *Phys. Rev. Lett.* **113**, 235902 (2014).
- [34] C. López, R. Rurali, and C. Cazorla, IonDiff: Command-line tool to identify ionic diffusion events and hopping correlations in molecular dynamics simulations, *J. Open Source Software* **9**, 6616 (2024).
- [35] C. López, R. Rurali, and C. Cazorla, <https://github.com/IonRepo/IonDiff>.
- [36] A. Emly, E. Kioupakis, and A. Van der Ven, Phase stability and transport mechanisms in antiperovskite Li_3OCl and Li_3OBr superionic conductors, *Chem. Mater.* **25**, 4663 (2013).
- [37] C. López, R. Rurali, and C. Cazorla, How concerted are ionic hops in inorganic solid-state electrolytes? *J. Am. Chem. Soc.* **146**, 8269 (2024).
- [38] H. T. Stokes and D. M. Hatch, FINDSYM: Program for identifying the space-group symmetry of a crystal, *J. Appl. Cryst.* **38**, 237 (2005).
- [39] C. Cazorla and J. Boronat, Simulation and understanding of atomic and molecular quantum crystals, *Rev. Mod. Phys.* **89**, 035003 (2017).
- [40] C. Cazorla, D. Errandonea, and E. Sola, High-pressure phases vibrational properties, and electronic structure of $\text{Ne}(\text{He})_2$ and $\text{Ar}(\text{He})_2$: A first-principles study, *Phys. Rev. B* **80**, 064105 (2009).
- [41] C. Cazorla and R. Rurali, Dynamical tuning of the thermal conductivity via magnetophonic effects, *Phys. Rev. B* **105**, 104401 (2022).
- [42] S. Ehsan, M. Arrigoni, G. K. H. Madsen, P. Blaha, and A. Tröster, First-principles self-consistent phonon approach to the study of the vibrational properties and structural phase transition of BaTiO_3 , *Phys. Rev. B* **103**, 094108 (2022).
- [43] C. Cazorla, S. Bichelmaier, C. Escorihuela-Sayalero, and R. Rurali, Light-driven dynamical tuning of the thermal conductivity in ferroelectrics, *Nanoscale* **16**, 8335 (2024).
- [44] R. Rurali, C. Escorihuela-Sayalero, J. Ll. Tamarit, J. Íñiguez-González, and C. Cazorla, Giant photocaloric effects across a vast temperature range in ferroelectric perovskites, *Phys. Rev. Lett.* **133**, 116401 (2024).
- [45] A. Carreras, A. Togo, and I. Tanaka, DynaPhoPy: A code for extracting phonon quasiparticles from molecular dynamics simulations, *Comput. Phys. Commun.* **221**, 221 (2017).
- [46] K. Tolborg, J. Klarbring, A. M. Ganose, and A. Walsh, Free energy predictions for crystal stability and synthesizability, *Digit. Discov.* **1**, 586 (2022).
- [47] G. Kresse and J. Furthmüller, Efficient iterative schemes for *ab initio* total-energy calculations using a plane-wave basis set, *Phys. Rev. B* **54**, 11169 (1996).
- [48] P. E. Blöchl, Projector augmented-wave method, *Phys. Rev. B* **50**, 17953 (1994).
- [49] A. Togo and I. Tanaka, First principles phonon calculations in materials science, *Scr. Mater.* **108**, 1 (2015).
- [50] J. Rodríguez-Carvajal, Recent advances in magnetic structure determination by neutron powder diffraction, *Physica B* **192**, 55 (1993).
- [51] M. Scheidgen, *et al.*, NOMAD: A distributed web-based platform for managing materials science research data, *J. Open Source Softw.* **8**, 5388 (2023).